PAPER

Hybrid spatio-spectral coherent adaptive compensation for line-scanning temporal focusing microscopy

IOP Publishing Journal of Physics D: Applied Physics
J. Phys. D: Appl. Phys. **52** (2019) 024001 (9pp) https://doi.org/10.1088/1361-6463/aae75b

Hybrid spatio-spectral coherent adaptive compensation for line-scanning temporal focusing microscopy

Yuanlong Zhang[1,3], Xinyang Li[1,3], Hao Xie[1], Lingjie Kong[2] and Qionghai Dai[1]

[1] Department of Automation, Tsinghua University, Beijing 100084, People's Republic of China
[2] State Key Laboratory of Precision Measurement Technology and Instruments, Department of Precision Instrument, Tsinghua University, Beijing 100084, People's Republic of China

E-mail: konglj@tsinghua.edu.cn

Received 5 August 2018, revised 26 September 2018
Accepted for publication 10 October 2018
Published 31 October 2018

Abstract

Line-scanning temporal focusing microscopy (LTFM) is promising for various biomedical studies, due to its higher imaging speed compared to the gold-standard point-scanning two-photon microscopy while maintaining the same axial confinement. However, LTFM is susceptible to deteriorated performances in excitation efficiency, penetration depth, and resolutions, as a result of wavefront distortions in deep-tissue imaging. Here, we report the hybrid spatio-spectral coherent adaptive compensation (HSSCAC), the first reported technique to fully correct the wavefront distortions in LTFM. Compared with the conventional hill-climbing method, HSSCAC can fully compensate the aberrations. We demonstrate the performance of HSSCAC in deep imaging of neurons in cleared mouse brains and *in vivo* dynamic imaging of microglias in living mouse brains.

Keywords: nonlinear microscopy, adaptive optics, biomedical imaging, temporal focusing

(Some figures may appear in colour only in the online journal)

1. Introduction

Multiphoton microscopy (MPM) is currently popular in *in vivo* imaging for biomedical studies, due to its advantages in deep penetration, 3D sectioning capability, and low phototoxicity, etc [1–6]. In conventional MPM, a tight focus of ultrafast pulses is formed to enhance the excitation photon density for signal generation from nonlinear optical phenomena. Thus the origins of emission signals is confined to the focus, ensuring that MPM is less susceptible to tissue scattering. And the imaging can be performed by scanning the focal plane with a 2D mechanical scanner. However, the inertia of mechanical scanners, such as galvo and resonant galvo, would limit the imaging speed of such point scanning MPM considering [7–9]. The low imaging speed hampers studies of most high-speed biological dynamics [10, 11]. Recently, temporal focusing microscopy (TFM) has been proposed, which can achieve optical sectioning and wide-field excitation simultaneously [12–14]. By introducing an angular dispersion to the excitation femtosecond pulses with a grating, a temporal focus occurs when different frequency components overlap, which only happens within the focal region of the objective lens and thus ensures the confinement of two-photon wide-field excitation with decent axial resolutions [15, 16]. Compared with the traditional point scanning MPM, TFM enables high-speed imaging by parallel excitation while maintaining the high axial confinement [17]. There are generally two modalities of TFM: planar-illumination TFM in which samples are illuminated by a plane [17–19], and line-scanning TFM in which samples are illuminated by a mechanically sweeping line [20, 21]. Compared with the former one where the spatial focusing is weak, line-scanning temporal focusing microscopy (LTFM) exhibits higher robustness to scattering and better axial-confinement [22, 23]. The good balance between

[3] These authors contributed equally to this work.

imaging speed and axial resolution makes LTFM ideal for various applications, including laser processing [24] and large-scale imaging of biological dynamics [25].

However, suffering from wavefront distortions induced by the random refraction and scattering in turbid samples, the excitation confinement of MPM progressively weakens as the penetration depth increases, which further deteriorates the signal contrast [26, 27]. For wavefront compensation, adaptive optics (AO) techniques, originally proposed in astronomy, was adopted in microscopy [28–35]. For planar-illumination TFM, Chang *et al* proposed a sensorless hill-climbing algorithm based AO to compensate the tissue induced distortion, which could improve the axial excitation effectively [26]. However, such algorithm is time-consuming and may fall into a local optimum instead of reaching the global optimum, as a result of serial optimizations [36]. To the best of our knowledge, no AO method has been proposed specifically for LTFM yet.

Here we propose the HSSCAC technique which searches for the globally optimized phase compensation in parallel in both spatial and spectral dimensions, specifically designed for LTFM for the first time. Firstly, we theoretically calculate the effects of wavefront distortions in LTFM and prove the principle of HSSCAC. Secondly, we numerically demonstrate that wavefront compensation in both spatial and spectral dimensions are more efficient than wavefront compensation in spectral domain only. Thirdly, we experimentally demonstrate that the proposed HSSCAC algorithm could fully recover the imaging quality but the hill-climbing algorithm may fail. We validate the improvement of imaging quality by imaging fluorescent microspheres under a random wavefront induced by a deformable mirror (DM). We further demonstrate the performance of HSSCAC in deep imaging of neurons in cleared mouse brains and *in vivo* dynamic imaging of microglia in living mouse brains.

2. Experimental setup and methods

2.1. System design

The schematic of our proposed system is illustrated in figure 1. The design introduces a DM into the LTFM setup for the compensation of wavefront distortion. The beam from an 80 MHz laser (Chameleon Discovery, Coherent) with the pulse duration of ~120 fs at the central wavelength of 920 nm is used for two-photon excitation. An electro-optical modulator (EOM) (M3202RM, Conoptics) controls the laser intensity. The laser beam is then expanded by 2.5× in diameter with a lens pair (L1: $f = 60$ mm, L2: $f = 150$ mm). The expanded laser beam is then scanned in the vertical direction with a 1D galvanometer (GVS211, Thorlabs) and focused to a thin line on the surface of the diffraction grating (Edmund Optics, 830 lines/mm) with a cylindrical lens ($f = 300$ mm). The incident angle to the grating is ~50° to ensure that the central wavelength of the 1st diffraction light is perpendicular to the grating surface. The spectrally-spread pulse is collimated with a collimating lens (L3: $f = 200$ mm) and modulated with a DM (PTT111, Iris AO) placing at the focal plane of L3. The DM has 37 segments, whose circumscribed diameters are 700 μm. The diameter of the incident 2D beam on the DM surface is about 3.5 mm, which matches the aperture of the DM. A 4*f* telescope (L4, L5, both of $f = 300$ mm) relays the modulated beam profile to the pupil plane of the objective (60×, 1.0 NA, water immersion, Olympus, LUMPLFLN60XW). A line-shaped laser beam is formed at the focal plane of the objective, of around 80 μm in length. For each scanning period, we capture the image based on an epi-fluorescence setup including a dichroic mirror (DMSP750B, Thorlabs), a bandpass filter (E510/80, Chroma), a 200 mm tube lens (L6, TTL200-A, Thorlabs), and an sCMOS (Zyla 5.5 plus, Andor). Three-dimensional imaging can be performed with the axial movement of the sample stage (M-VP-25XA-XYZL, Newport).

2.2. Theoretical model of the proposed HSSCAC method

In this section, we will firstly calculate the excited signal intensity under distorted wavefronts on the sample, then derive algorithm to calculate the distorted phases in parallel.

The laser beam in LTFM is expanded in both spatial and spectral dimensions and fulfill the back pupil of the objective, as shown in the inset of figure 1(a). Thus DM could be modulated in both the spatial dimension (along the y-axis) and the spectral dimension (along the x-axis). Such relationship between x-axis and the spectral dimension could be described by the the light field at the back pupil of the objective [15]:

$$U_{\text{pupil}}(x, y, \omega) \propto e^{-\frac{(x-\alpha\omega)^2}{s^2}} e^{-\frac{y^2}{s^2+\alpha^2\Omega^2}} e^{-\frac{\omega^2}{\Omega^2}}, \tag{1}$$

here $(x,\ y)$ is the cartesian coordinate of the input pupil plane, ω is the beam frequency and α is a constant proportional to the groove density of the grating and the focal length of L3 [16]. $\sqrt{2\ln 2}\cdot\Omega$ is the full-width half maximum (FWHM) of the frequency spectrum of the pulse and $\sqrt{2\ln 2}\cdot s$ is the FWHM of each monochromatic beam in space. It can be seen that different spectral components are restricted around position $\alpha\omega$ along x-axis, as shown in figure 1(a). Thus the DM could modulate spectral phases when it works on x-y dimensions of the beam profile.

Assume that there is a piece-constant spatio-spectral wavefront aberration on the pupil plane, thus the distorted light field could be approximated as

$$U'_{\text{pupil}} = \sum_{m=1}^{N} e^{i\phi_m} P_m(x,\ y)\, U_{\text{pupil}}(x, y, \omega), \tag{2}$$

$$P_m(x, y) = \begin{cases} 1, \text{if} & (x, y) \in O_m \\ 0, \text{if} & (x, y) \notin O_m \end{cases}, \tag{3}$$

where ϕ_m is the sptaially specific distorted phase and $P_m(x, y)$ is the support function. O_m divides the back pupil into N segments and $\cup_{m=1}^{N} O_m$ fullfills the back pupil. By transforming U'_{pupil} to the focal plane, we could get the light field near the focal plane in the time domain [15]:

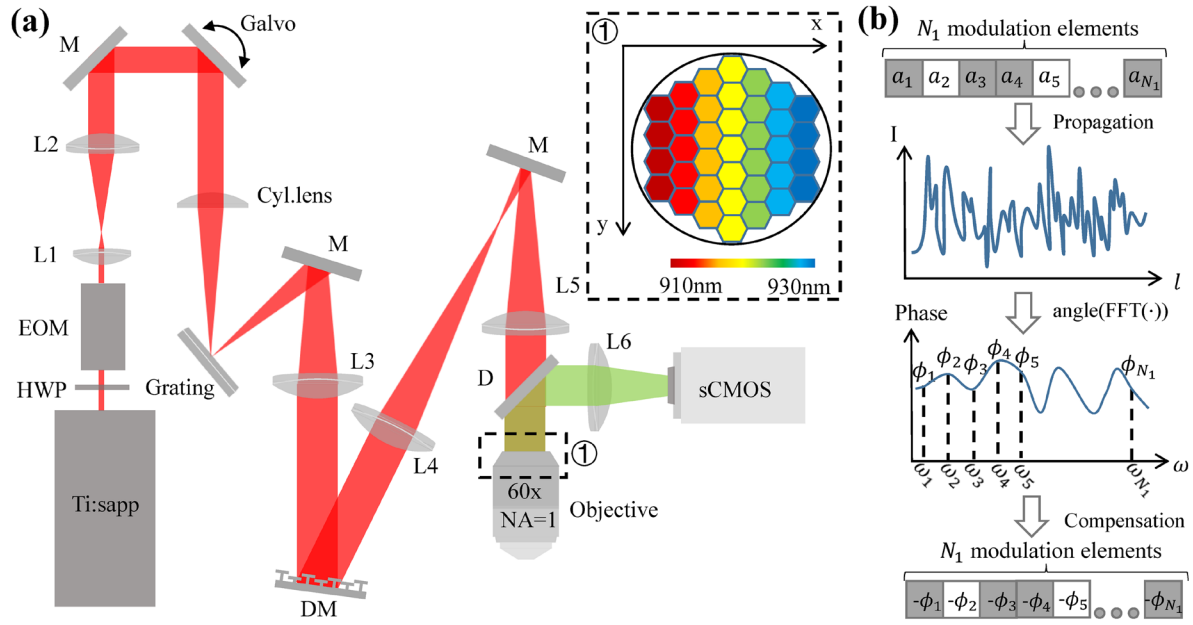

Figure 1. (a) Diagrams of the system setup. The pulse intensity is modulated with an electro-optical modulator (EOM). After expansion (by L1 and L2), the beam is firstly compressed to a line at the grating surface with the cylinder lens and then spatially chirped by the grating. The spatio-spectral profile is modulated by a deformable mirror (DM) and then focused by the objective. The excited fluorescent signals are recorded by the sCMOS. Inset, the spatio-spectral distribution of the beam on back pupil of the objective (conjugated with the surface of DM). (b) Schematic of the parallel compensation algorithm for LTFM. The Symbols: HWP, half wave plate; Cyl. Lens, cylinder lens; M, reflective mirror; D, dichroic mirror.

$$U'_{\text{focal}} \propto e^{-\frac{t^2}{\tau^2_{\text{sweep}}}} \sum_{m=1}^{N} e^{i\phi_m} h_m\left(x'' + v_{\text{sweep}}t,\ y'', z''\right), \quad (4)$$

where

$$h_m = \iint P_m\left(x',\ y'\right) P\left(x',\ y'\right) e^{-\frac{x'^2+y'^2}{\alpha^2+\alpha^2\Omega^2}} \times e^{ik_0\left(\frac{x''x'+y''y'}{f} + z''\frac{x'^2+y'^2}{f^2}\right)} \mathrm{d}x'\mathrm{d}y'. \quad (5)$$

Here v_{sweep} and τ_{sweep} are independent of the spatial coordinates (x'', y'', z'') and determined by the system. t represents time. $P\left(x', y'\right)$ is the pupil function of the objective. The two-photon emission (TPE) signal is proportional to the forth power of the light field and could be written as

$$\text{TPE} \propto C_1 \iint \left| \sum_{m=1}^{N} e^{i\phi_m} h_m\left(x'',\ y'', z''\right) \right|^4 \mathrm{d}x''\mathrm{d}y'', \quad (6)$$

where C_1 is independent of z''.

Now if we add linearly increasing phase to some of the pieces on the pupil [37, 38], as shown in the figure 1(b), the modulated light field could be written as

$$U''_{\text{pupil}}\left(l\right) = \sum_{m=1}^{N_1} e^{i(\phi_m + a_m l)} P_m\left(x,\ y\right) U_{\text{pupil}}\left(x, y, t\right) + \sum_{m=N_1+1}^{N} e^{i\phi_m} P_m\left(x, y\right) U_{\text{pupil}}\left(x, y, t\right), \quad (7)$$

here a_m is the increasing ratio of the linear modulation and l represents the modulations. We assume that

$$\begin{cases} a_m + a_n > a_l \\ a_m - a_n < a_l \end{cases}, \forall m, n, l \in [1, \ldots N_1]. \quad (8)$$

Note that $N_1 < N$. The modulated intensity signal could be written as the sum of different modulation segments [39],

$$\begin{aligned} &\text{TPE}'\left(l\right) \\ &\propto C_2 \iint \left| \sum_{m=1}^{N_1} e^{i(\phi_m + a_m l)} h_m\left(x'',\ y'', z''\right) + \sum_{n=N_1+1}^{N} e^{i\phi_n} h_n\left(x'',\ y'', z''\right) \right|^4 \mathrm{d}x''\mathrm{d}y'' \\ &= \sum_{m=1}^{N_1} C^{(m)} \cos\left(a_m l + \phi_m - \Phi_r\right) + C_3, \end{aligned} \quad (9)$$

where $C^{(m)}$ is segment-specific constant and C_3 is the combination of components with frequency not included $a_m|_{1\ldots N_1}$. Φ_{r} is a combination of $\phi_n|_{N_1+1\ldots N}$ and keeps constant while modulating the first N_1 segments. If we apply Fourier transform to $\text{TPE}'\left(l\right)$ with respect to the variable l, then $\phi_m - \Phi_{\text{r}}$ could be directly read out from the angle information of the $\text{TPE}'\left(l\right)$ in the frequency domain, as the figure 1(b) shows [40]. The achieved phases are then sign reversed and applied to the corresponding modulated segments. The second step is to exchange the modulated element group (the N_1 elements) with the unmodulated element group (the remaining $N - N_1$ elements) and repeat the modulation and calculation procedure, thus all the compensation phases could be determined. Note that Φ_{r} depends on the initial aberration of the system and thus could be different in the two steps. Benefiting from the nonlinearity in TPE, it can reach a convergence after several iterations of these two steps [41].

From the calculation above, it can be seen that the proposed HSSCAC algorithm is accurate (i.e. can reach the global optimum) under the assumption of piece-constant spatio-spectral phase aberration, and is independent of the initial phases. In contrast, in the hill-climbing algorithm, the initial phases would significantly affect the convergence [42].

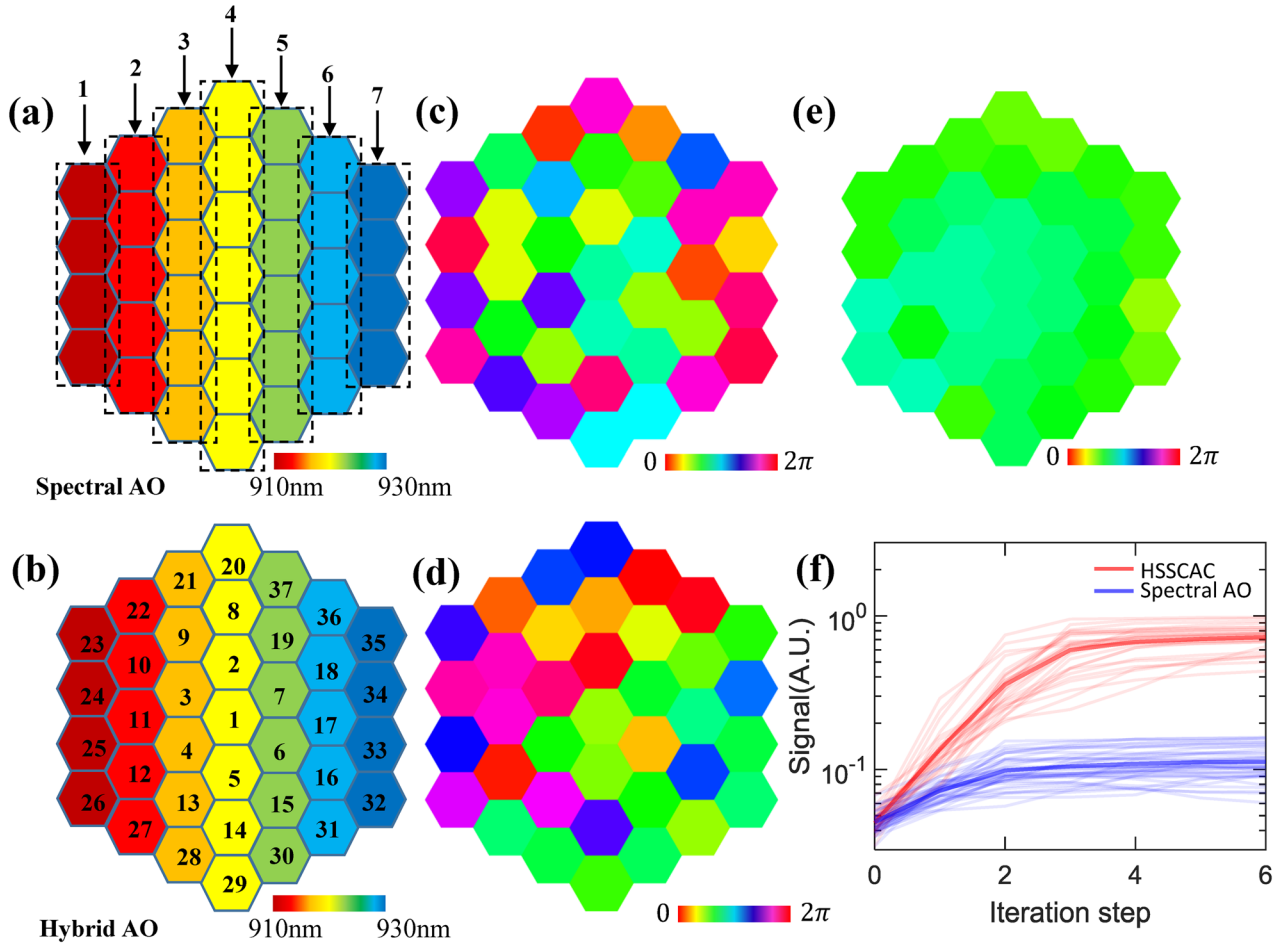

Figure 2. Comparison of spectral AO and hybrid AO (HSSCAC) via numerical simulations. (a) Spectral AO: dividing the back pupil of the objective (conjugation to the DM) into seven segments corresponding to the spectral profile. (b) Hybrid AO: dividing the back pupil of the objective into 37 segments corresponding to the spatio-spectral profile. (c) Preloaded spatio-spectral phase distortion. (d) Residual phase after spectral AO compensation. (e) Residual phase after hybrid spatio-spectral AO compensation. (f) Intensities improvement with iterations (30 trials, signal under flatten phase is 1). Red, HSSCAC; blue, spectral AO.

Besides, the phase for each wavefront segment is determined independently and in parallel in our HSSCAC method, which will lead to a faster measurement and compensation procedure. However, the hill-climbing algorithm can only work in serial.

3. Experimental results

All procedures involving mice were approved by the Animal Care and Use Committees of Tsinghua University.

3.1. Validation of the superior performance of HSSCAC compared with the spectral AO method

As shown in section 2.2, different segmentation strategies would affect the compensation results with the proposed algorithm. Here we perform numerical simulations to demonstrate that the proposed algorithm shows superior performances in compensating in both spatial and spectral dimensions simultaneously (spatio-spectral segmentations, HSSCAC method) than compensating in the spectral dimension only (spectral segmentations, spectral AO) as in [26]. For spectral AO compensation, the total 37 elements of the DM are arranged into seven segments to modulate the phase of seven spectral components correspondingly, as shown in the figure 2(a). For HSSCAC, the total 37 elements of the DM are modulated independently as shown in the figure 2(b). After loading the initial wavefront distortion (shown in the figure 2(c)) to the back pupil of the objective, the distorted light field propagates through the objective as described in the Fresnel diffraction [43], then forms a focus [44]. In both cases, the algorithm is run for three rounds (i.e. iterations) [40, 45]. Figures 2(d) and (e) show the residual phase with the spectral AO method and the HSSCAC method, respectively. We could see that the HSSCAC method could fully compensate the distortion and retrieve a flatten phase, while the spectral AO method could only compensate parts of the distorted phase. We repeat the simulations for 30 times with different random initial wavefront distortions and record the intensity improvements with iteration steps in figure 2(f) (we define the signal under flatten phase to be 1). It is shown that the increasing curve of the HSSCAC method is much steeper than that of the spectral AO method, and HSSCAC could fully retrieve the signal intensity with no wavefront distortions. Note that, due to the

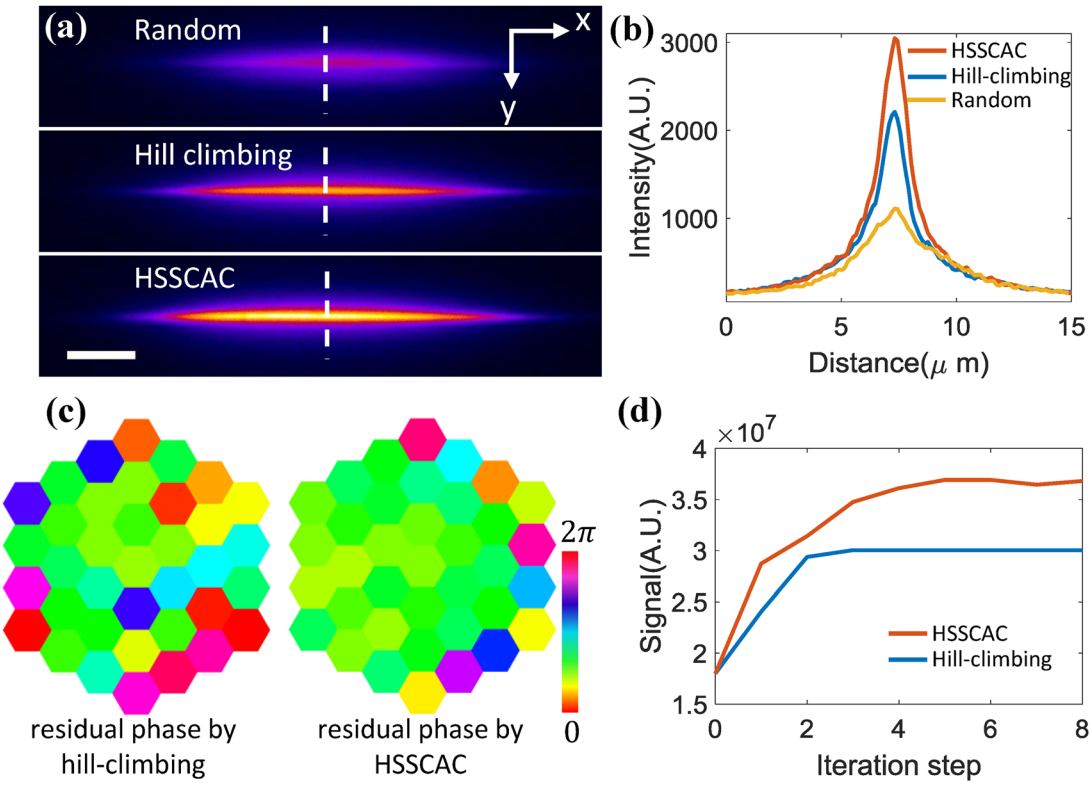

Figure 3. (a) Imaging results under a random initial wavefront, with the hill-climbing algorithm and the HSSCAC. (b) Intensity profiles along the dashed line in (a). Red, HSSCAC; blue, hill-climbing; yellow, the random initial phase. (c) Residual phase after hill-climbing (left) and HSSCAC (right). (d) Intensities increase with iteration step. Red, HSSCAC; blue, hill-climbing. (d). Scale bar: 15 μm.

discretization in the simulation, some trials converge to lower signal intensities than 1, while most of the trials succeeds to reach the ideal plateau.

3.2. Validation of the global optimum performance of HSSCAC

We further experimentally demonstrate that HSSCAC could fully compensate the wavefront distortion. In contrast, the hill-climbing method [26] may fail.

For the HSSCAC method, we sets 5 ms for each modulation and another 5 ms for the camera to capture images (by selecting a small ROI in the sCMOS). For the DM of 37 modulation elements employed in our experiment, the minimum number of phase modulations required is 74 according to the Nyquist–Shannon theorem. In practical experiments, we perform 148 measurements. We divide all the elements randomly into two groups with $N_1 = 18$. One group is modulated while the other group is kept stationary. We run three iterations (i.e. six modulation steps). At the end of each modulation step, the recorded nonlinear fluorescent signal is Fourier transformed and the achieved phase profile is sign reversed and applied to the modulated group.

For the hill-climbing method, all the 37 segments are used, but the phase measurement is achieved as below [26]: we apply variable phases stepwisely (step by $\pi/10$, from 0 to 2π) onto every segment, then position them at the phases corresponding to the maximum image intensity during the measurements. Note that in this condition, the number of measurements for the hill-climbing method is 370, which is sufficient to ensure the measurement accuracy but would cost two times longer than that of the HSSCAC method.

We preload a random wavefront to the DM and park the galvo at the center of the FOV to capture the static line-excitation from a fluorescent plastic plate (Chroma). Figure 3(a) shows the captured line-excitation patterns with a random wavefront, the compensation wavefront calculated with the hill-climbing algorithm, and the compensation wavefront calculated with HSSCAC. From the intensity profile along the dashed line in figure 3(b), it can be seen that HSSCAC could improve the fluorescent signal higher than that of the hill-climbing method. Furthermore we check the residual wavefront after running both methods and find that there remains some random distortions after compensation with the hill-climbing method. In contrast, the residual wavefront distortion of HSSCAC is minor, induced by the nonuniformity of the excitation beam (the intensity in the right border of the DM is quite low, thus the phase compensation there affects much less than the other area). The failure of the hill-climbing method could also be seen from the signal increasing curve in figure 3(d), where it reaches a plateau much earlier at a lower signal intensity (i.e. it falls into a local optimum but missed the global one). In comparison, HSSCAC is independent of the initial phase and could reach the global optimum every time.

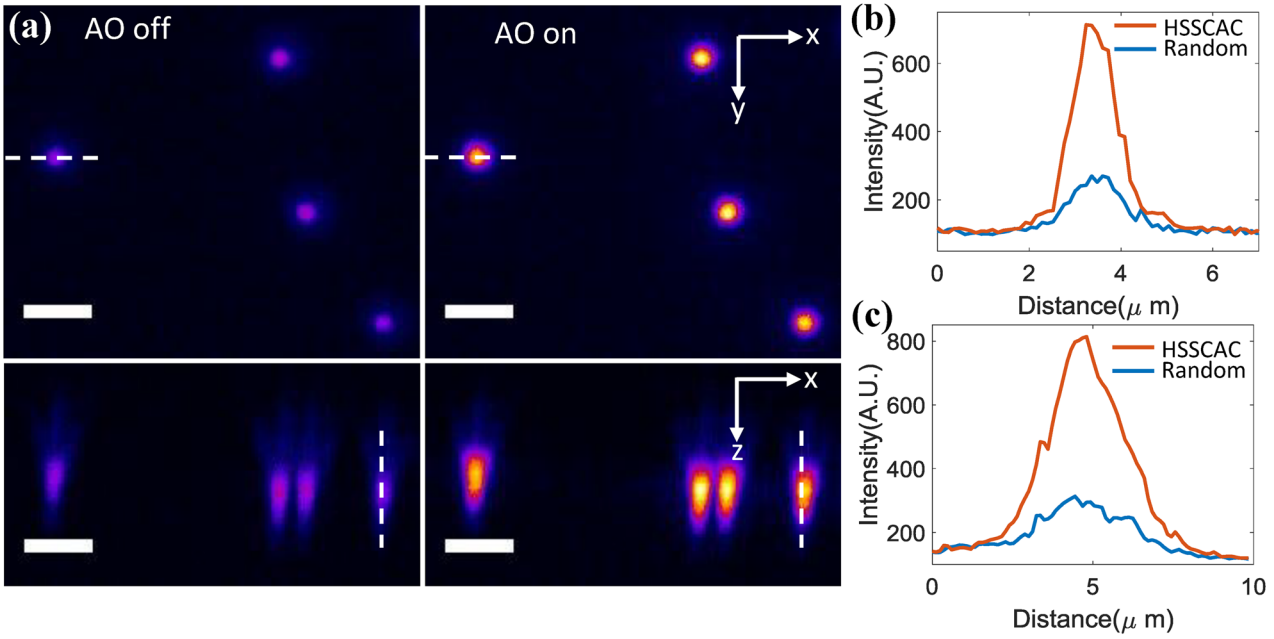

Figure 4. (a) Imaging results of 1 μm fluorescent microspheres with and without the HSSAC algorithms under a random initial phase. (b) Intensity along the marked lines in *x*-*y* plane. (c) Intensity along the marked lines in *x*-*z* plane. Scale bar in a: 5 μm. Legends in (b) and (c): red, HSSCAC; blue, a random initial wavefront.

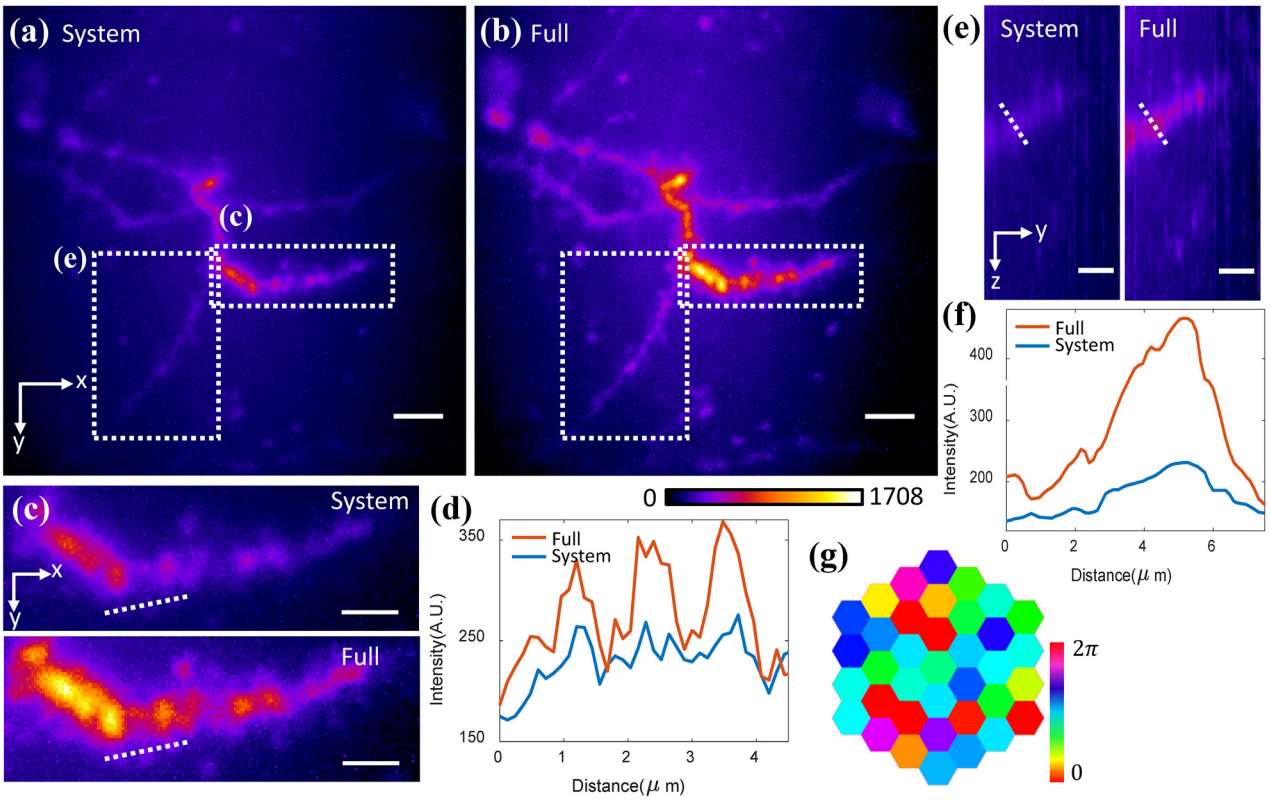

Figure 5. (a) and (b) MIPs along the *z*-axis of a 40 μm-thick image stack (400–440 μm deep) acquired with the system and full correction, respectively. (c) Zoom-in view of the dashed box in (a) and (b). (d) Intensity profiles along the marked lines in (c). (e) MIPs along *x*-axis of a 12 μm thick *y*-*z* stack (marked by the dashed box in (a)) acquired with the system (left) and full AO correction (right). MIPs of *y*-*z* stack are shown with the bilinear interpolation along *z*-axis to equate the lateral and axial pixel sizes. (f) Intensity profiles along the indicated lines in (e). (g) Wavefront pattern for full compensation. Scale bar: 5 μm in (a), (b) and (e); 2.5 μm in (c). Legends in (d) and (f): red, full correction; blue, system correction.

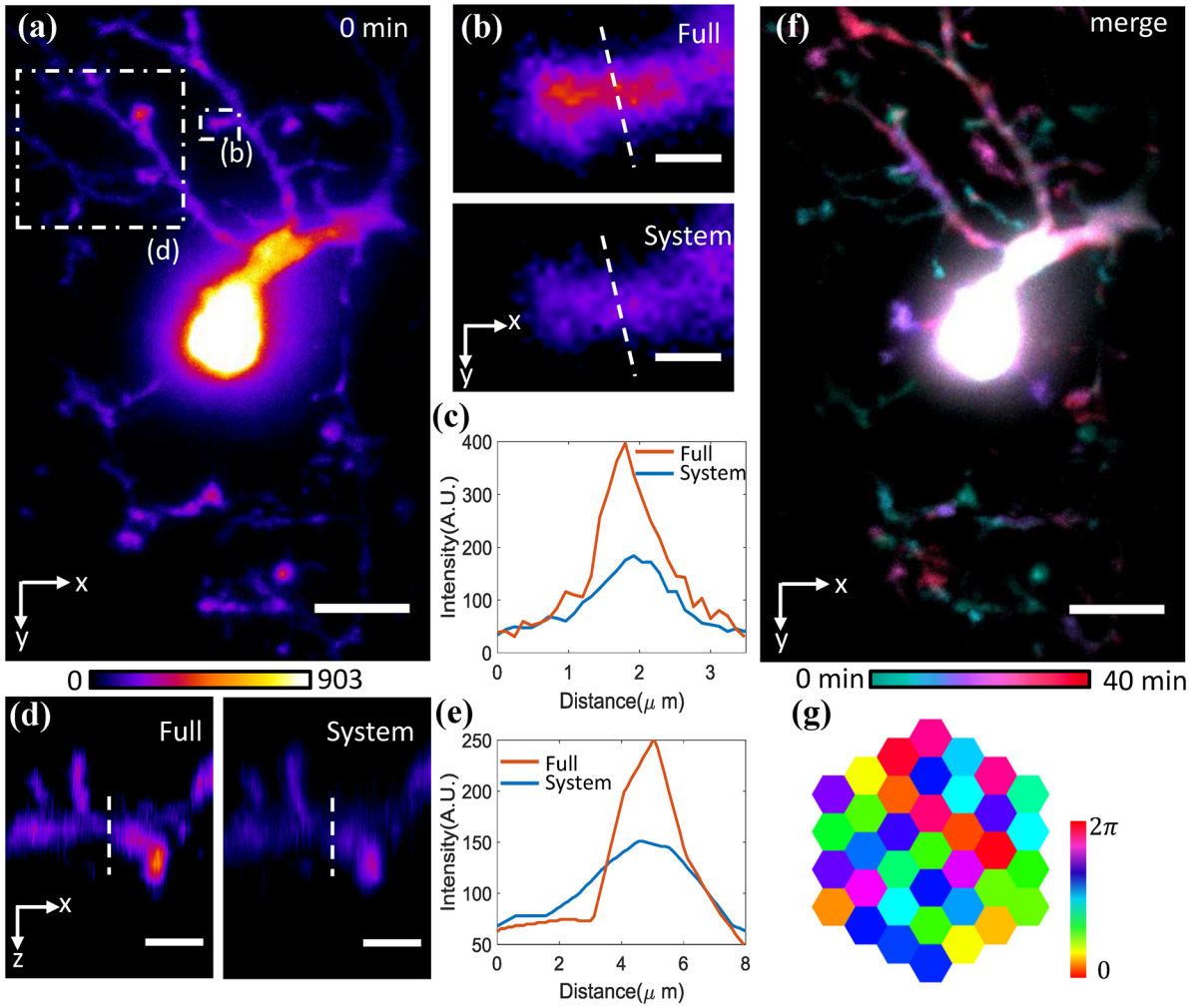

Figure 6. (a) MIP along z-axis of a 25 μm-thick image stack (110–135 μm under the dura) acquired with the HSSCAC algorithm. (b) Zoom-in views of lateral area marked by the dashed box in (a) with full correction (upper) and system correction (lower), respectively. (c) Intensity profiles along the indicated lines in (b). (d) MIPs along y-axis of an 18 μm thick x-z stack (marked by the dashed box in (a)) acquired with full correction (left) and with system correction (right), respectively. The MIPs of x-z stacks are shown with bilinear interpolation along z-axis to equate the lateral and axial pixel sizes. (e) Intensity profiles along the indicated lines in (d). (f) Dynamics of the microglia in 40 min (with 10 min interval), merged with different colors. (g) Wavefront pattern for full correction. Scale bars in (a) and (d) and (f) are 10 μm, in (b) is 2 μm. Legends in (c) and (e): red, full correction; blue, system correction.

3.3. Imaging results with fluorescent microspheres

Then we demonstrate the effectiveness of HSSCAC in imaging fluorescent microspheres. We first add a random initial wavefront to the DM, then run HSSCAC. Figure 4(a) shows the maximum intensity projection (MIP) of 1 μm microspheres (T14792, Thermo Fisher) along z-axis (MIP of a 15 μm x-y stack) and along y-axis (MIP of a 30 μm x-z stack). It can be seen that with HSSCAC, the fluorescent signals are much stronger compared with the images without AO compensation. In figures 4(b) and (c), we quantitatively compare the intensities in lateral and axial planes by drawing the intensity profiles along the dashed lines in figure 4(a), and show the obvious improvement.

3.4. Deep imaging of neurons in Thy1-YFP mouse brains after tissue clarity

We image the cleared brains of the Thy1-YFP (H line) mice (JAX No. 003782) by uDISCO (ultimate 3D imaging of solvent-cleared organs) to further investigate the effectiveness of HSSCAC technique in the imaging of biological tissues [46]. The mice are deeply anesthetized, and perfused with phosphate buffered saline (pH 7.4) followed by 4% paraformaldehyde for fixation. The brains are dissected and cut into 1 mm coronal slices after overnight fixation. The slices are sequentially dehydrated in a series of tert-butanol (30%, 50%, 70%, 80%, 90%, 96%, and 100%, 2 h for each step) at room temperature. The dehydrated slices are incubated in BABB-D4 (BABB: benzyl alcohol/benzyl benzoate = 1/2, BABB-D4: BABB/diphenyl ether = 4/1) for more than 1 h at room temperature until they become optically transparent.

We take imaging at ~400 μm depth under the surface of the slices, and show the MIPs of a 40 μm thick x-y image stack with system correction (correction of system induced aberration) and full correction (correction of both system and sample induced aberrations), with HSSCAC in figures 5(a) and (b), respectively. It can be seen that signals in the image achieved with HSSCAC are much stronger. In figure 5(c), we show that

spines on the dendrite are much clearer with HSSCAC. In figure 5(d), we also show that HSSCAC can resolve the fine structures along the dendrite marked by the white dashed line in figure 5(c). In figure 5(e), we show MIPs along x-axis of a 12 μm thick y-z image stack (marked by the dashed white box in (a)). The corresponding intensity profiles along the indicated lines in figure 5(e) are shown in figure 5(f), which shows that HSSCAC can increase the signal intensity obviously. The full compensation phase pattern is shown in the figure 5(g).

3.5. *In vivo dynamic imaging of CX3CR1-GFP mice*

We also demonstrate the performance of the proposed technique in *in vivo* imaging of living Cx3Cr1-GFP mouse (JAX No. 005582) brains. After craniotomy, we conduct acute imaging with the living mice under shallow anesthesia [28] by continuous inhalation of isoflurane and being head-restrained under the objective. In figure 6(a), we show the MIP along the z-axis of a 25 μm-thick image stack (110–135 μm under the dura) acquired with the HSSCAC technique. By comparing the intensities of fine processes of the microglia, we could see that HSSCAC could apparently improve the signal level, which enables us to easily resolve the structures, as shown in figures 6(b). In figure 6(c), we quantitatively compare the signal improvement along the dashed line in figure 6(b) with system correction and full correction using the HSSCAC algorithm. Figure 6(d) shows the MIP along the y-axis of an 18 μm-thick x-z image stack (marked by the dashed box in figure 6(a)). The corresponding intensity profiles along the indicated lines are shown in figure 6(e). It can be seen that the signals are much higher after full correction. We also perform time-lapse imaging of the microglia dynamics in 40 min after performing HSSCAC, as shown in figure 6(f) where morphologies at different time points are color coded. It can be seen the measured wavefront for compensation is still valid after 40 min at least. Figure 6(g) is the wavefront pattern for full correction measured by HSSCAC, which is complex due to the strong scattering of the mouse brain.

4. Discussion and conclusion

The HSSCAC algorithm can effectively enhance the signals in deep tissue imaging. Limited by the low energy of femtosecond pulses available from our laser source, we only demonstrated the proof-of-concept experiments. To perform imaging at larger penetration depths with higher signal-to-noise ratios, a femtosecond laser of a low repetition rate but a high pulse energy would help.

In summary, we have demonstrated the HSSCAC algorithm that could fully compensate wavefront distortions in LTFM, for the first time. Through both simulations and experiments, we show that the HSSCAC algorithm performs better than the spectral AO method, and can retrieve the global optimized compensation while the hill-climbing algorithm may fail. We further validated the performance improvement of HSSCAC in deep imaging of neurons in cleared mouse brains and *in vivo* dynamic imaging of microglia in living mouse brains.

Acknowledgments

YZ thanks Yingjun Tang and Xiaofei Han for sample preparations. LK thanks the support from Tsinghua University and the 'Thousand Talents Plan' Youth Program. The authors thank the fund from the National Natural Science Foundation of China (NSFC) (No. 61771287, No. 61327902, and No. 61741116).

ORCID iDs

Lingjie Kong https://orcid.org/0000-0002-8250-7547

References

[1] Denk W, Strickler J and Webb W 1990 Two-photon laser scanning fluorescence microscopy *Science* **248** 73–6
[2] Helmchen F and Denk W 2005 Deep tissue two-photon microscopy *Nat. Methods* **2** 932–40
[3] Svoboda K and Yasuda R 2006 Principles of two-photon excitation microscopy and its applications to neuroscience *Neuron* **50** 823–39
[4] Yang W and Yuste R 2017 *In vivo* imaging of neural activity *Nat. Methods* **14** 349–59
[5] Ji N, Freeman J and Smith S L 2016 Technologies for imaging neural activity in large volumes *Nat. Neurosci.* **19** 1154–64
[6] Bewersdorf J, Pick R and Hell S W 1998 Multifocal multiphoton microscopy *Opt. Lett.* **23** 655–7
[7] Botcherby E J, Smith C W, Kohl M M, Debarre D, Booth M J, Juskaitis R, Paulsen O and Wilson T 2012 Aberration-free three-dimensional multiphoton imaging of neuronal activity at kHz rates *Proc. Natl Acad. Sci. USA* **109** 2919–24
[8] Bar-Noam S, Farah N and Shoham S 2016 Correction-free remotely scanned two-photon *in vivo* mouse retinal imaging *Light: Sci. Appl.* **5** e16007
[9] Kirkpatrick N D, Chung E, Cook D C, Han X, Gruionu G, Liao S, Munn L L, Padera T P, Fukumura D and Jain R K 2012 Video-rate resonant scanning multiphoton microscopy: an emerging technique for intravital imaging of the tumor microenvironment *Intravital* **1** 60–8
[10] Yang W, Miller J E, Carrillo-Reid L, Pnevmatikakis E, Paninski L, Yuste R and Peterka D S 2016 Simultaneous multi-plane imaging of neural circuits *Neuron* **89** 269–84
[11] Kong L, Tang J, Little J P, Yu Y, Lammermann T, Lin C P, Germain R N and Cui M 2015 Continuous volumetric imaging via an optical phase-locked ultrasound lens *Nat. Methods* **12** 759–62
[12] Oron D and Silberberg Y 2005 Spatiotemporal coherent control using shaped, temporally focused pulses *Opt. Express* **13** 9903–8
[13] Oron D, Tal E and Silberberg Y 2005 Scanningless depth-resolved microscopy *Opt. Express* **13** 1468–76
[14] Zhu G, van Howe J, Durst M, Zipfel W and Xu C 2005 Simultaneous spatial and temporal focusing of femtosecond pulses *Opt. Express* **13** 2153–9
[15] Durst M E, Zhu G and Xu C 2008 Simultaneous spatial and temporal focusing in nonlinear microscopy *Opt. Commun.* **281** 1796–805
[16] Durst M E, Zhu G and Xu C 2006 Simultaneous spatial and temporal focusing for axial scanning *Opt. Express* **14** 12243–54
[17] Prevedel R *et al* 2016 Fast volumetric calcium imaging across multiple cortical layers using sculpted light *Nat. Methods* **13** 1021–8

[18] Yih J N, Hu Y Y, Sie Y D, Cheng L C, Lien C H and Chen S J 2014 Temporal focusing-based multiphoton excitation microscopy via digital micromirror device *Opt. Lett.* **39** 3134–7
[19] Schrodel T, Prevedel R, Aumayr K, Zimmer M and Vaziri A 2013 Brain-wide 3D imaging of neuronal activity in Caenorhabditis elegans with sculpted light *Nat. Methods* **10** 1013–20
[20] Li Z, Hou J, Suo J, Qiao C, Kong L and Dai Q 2017 Contrast and resolution enhanced optical sectioning in scattering tissue using line-scanning two-photon structured illumination microscopy *Opt. Express* **25** 32010–20
[21] Park J, Rowlands C and So P 2017 Enhanced axial resolution of wide-field two-photon excitation microscopy by line scanning using a digital micromirror device *Micromachines* **8** 85
[22] Dana H, Kruger N, Ellman A and Shoham S 2013 Line temporal focusing characteristics in transparent and scattering media *Opt. Express* **21** 5677–87
[23] Sela G, Dana H and Shoham S 2013 Ultra-deep penetration of temporally-focused two-photon excitation *Proc. SPIE* **8588** 858824
[24] Sun B, Salter P S, Roider C, Jesacher A, Strauss J, Heberle J, Schmidt M and Booth M J 2018 Four-dimensional light shaping: manipulating ultrafast spatiotemporal foci in space and time *Light: Sci. Appl.* **7** 17117
[25] Dana H, Marom A, Paluch S, Dvorkin R, Brosh I and Shoham S 2014 Hybrid multiphoton volumetric functional imaging of large-scale bioengineered neuronal networks *Nat. Commun.* **5** 3997
[26] Chang C Y, Cheng L C, Su H W, Hu Y Y, Cho K C, Yen W C, Xu C, Dong C Y and Chen S J 2014 Wavefront sensorless adaptive optics temporal focusing-based multiphoton microscopy *Biomed. Opt. Express* **5** 1768–77
[27] Ji N 2017 Adaptive optical fluorescence microscopy *Nat. Methods* **14** 374–80
[28] Park J H, Kong L, Zhou Y and Cui M 2017 Large-field-of-view imaging by multi-pupil adaptive optics *Nat. Methods* **14** 581–3
[29] Zheng W *et al* 2017 Adaptive optics improves multiphoton super-resolution imaging *Nat. Methods* **14** 869–72
[30] Wang K, Milkie D E, Saxena A, Engerer P, Misgeld T, Bronner M E, Mumm J and Betzig E 2014 Rapid adaptive optical recovery of optimal resolution over large volumes *Nat. Methods* **11** 625–8
[31] Booth M J 2006 Wavefront sensorless adaptive optics for large aberrations *Opt. Lett.* **32** 5–7
[32] Rueckel M, Mack-Bucher J A and Denk W 2006 Adaptive wavefront correction in two-photon microscopy using coherence-gated wavefront sensing *Proc. Natl Acad. Sci. USA* **103** 17137–42
[33] Débarre D, Botcherby E J, Booth M J and Wilson T 2008 Adaptive optics for structured illumination microscopy *Opt. Express* **16** 9290–305
[34] Hell S W *et al* 2015 The 2015 super-resolution microscopy roadmap *J. Phys. D: Appl. Phys.* **48** 443001
[35] Rodriguez C and Ji N 2018 Adaptive optical microscopy for neurobiology *Curr. Opin. Neurobiol.* **50** 83–91
[36] Koutsoupias E and Papadimitriou C H 1992 On the greedy algorithm for satisfiability *Inf. Process. Lett.* **43** 53–5
[37] Cui M 2011 A high speed wavefront determination method based on spatial frequency modulations for focusing light through random scattering media *Opt. Express* **19** 2989–95
[38] Kong L and Cui M 2015 *In vivo* neuroimaging through the highly scattering tissue via iterative multi-photon adaptive compensation technique *Opt. Express* **23** 6145–50
[39] Liu R, Milkie D E, Kerlin A, MacLennan B and Ji N 2014 Direct phase measurement in zonal wavefront reconstruction using multidither coherent optical adaptive technique *Opt. Express* **22** 1619–28
[40] Bridges W B, Brunner P T, Lazzara S P, Nussmeier T A, O'Meara T R, Sanguinet J A and Brown W P Jr 1974 Coherent optical adaptive techniques *Appl. Opt.* **13** 291–300
[41] Aviles-Espinosa R, Andilla J, Porcar-Guezenec R, Olarte O E, Nieto M, Levecq X, Artigas D and Loza-Alvarez P 2011 Measurement and correction of *in vivo* sample aberrations employing a nonlinear guide-star in two-photon excited fluorescence microscopy *Biomed. Opt. Express* **2** 3135–49
[42] Mitchell M, Holland J H and Forrest S 1994 When will a genetic algorithm outperform hill climbing *6th International Conference on Neural Information Processing System* pp 51–8
[43] Goodman J W 2008 *Introduction to Fourier Optics* (New York: W H Freeman)
[44] Wolf E and Born M 1980 *Principles of Optics* (New York: Cambridge University Press)
[45] Cui M 2011 Parallel wavefront optimization method for focusing light through random scattering media *Opt. Lett.* **36** 870–2
[46] Pan C, Cai R, Quacquarelli F P, Ghasemigharagoz A, Lourbopoulos A, Matryba P, Plesnila N, Dichgans M, Hellal F and Erturk A 2016 Shrinkage-mediated imaging of entire organs and organisms using uDISCO *Nat. Methods* **13** 859–67